

# Characterization of Electron Beam Free-Form Fabricated 2219 Aluminum and 316 Stainless Steel

## *Abstract*

*Researchers at NASA Langley Research Center have developed an additive manufacturing technology for ground and future space based applications. The electron beam free form fabrication (EBF3) is a rapid metal fabrication process that utilizes an electron beam gun in a vacuum environment to replicate a CAD drawing of a part. The electron beam gun creates a molten pool on a metal substrate, and translates with respect to the substrate to deposit metal in designated regions through a layer additive process. Prior to demonstration and certification of a final EBF3 part for space flight, it is imperative to conduct a series of materials validation and verification tests on the ground in order to evaluate mechanical and microstructural properties of the EBF3 manufactured parts. Part geometries of EBF3 2219 aluminum and 316 stainless steel specimens were metallographically inspected, and tested for strength, fatigue crack growth, and fracture toughness. Upon comparing the results to conventionally welded material, 2219 aluminum in the as fabricated condition demonstrated a 30% and 16% decrease in fracture toughness and ductility, respectively. The strength properties of the 316 stainless steel material in the as deposited condition were comparable to annealed stainless steel alloys. Future fatigue crack growth tests will integrate various stress ranges and maximum to minimum stress ratios needed to fully characterize EBF3 manufactured specimens.*

# Characterization of Electron Beam Free-Form Fabricated 2219 Aluminum and 316 Stainless Steel

Yasamin Ekrami<sup>1</sup>

*NASA Lyndon B. Johnson Space Center, Houston, TX, 77058*

Scott C. Forth, Ph.D.<sup>2</sup> and Michael C. Waid<sup>3</sup>

*NASA Lyndon B. Johnson Space Center, Houston, TX, 77058*

Researchers at NASA Langley Research Center have developed an additive manufacturing technology for ground and future space based applications. The electron beam free form fabrication (EBF3) is a rapid metal fabrication process that utilizes an electron beam gun in a vacuum environment to replicate a CAD drawing of a part. The electron beam gun creates a molten pool on a metal substrate, and translates with respect to the substrate to deposit metal in designated regions through a layer additive process. Prior to demonstration and certification of a final EBF3 part for space flight, it is imperative to conduct a series of materials validation and verification tests on the ground in order to evaluate mechanical and microstructural properties of the EBF3 manufactured parts. Part geometries of EBF3 2219 aluminum and 316 stainless steel specimens were metallographically inspected, and tested for strength, fatigue crack growth, and fracture toughness. Upon comparing the results to conventionally welded material, 2219 aluminum in the as fabricated condition demonstrated a 30% and 16% decrease in fracture toughness and ductility, respectively. The strength properties of the 316 stainless steel material in the as deposited condition were comparable to annealed stainless steel alloys. Future fatigue crack growth tests will integrate various stress ranges and maximum to minimum stress ratios needed to fully characterize EBF3 manufactured specimens.

## Nomenclature

$\Delta\sigma$	= stress range
$K$	= fracture mechanics stress-intensity factor
$K_c$	= critical stress intensity factor for fracture
$\Delta K$	= stress intensity factor range
$R$	= ratio of minimum K to maximum K in given cycle
$a$	= crack length
$w$	= width
$t$	= plate thickness
$N$	= cycle number
$da/dN$	= crack extension per cycle of load
$n$	= sample size
$EBF^3$	= Electron Beam Free-form Fabrication
$LEFM$	= linear elastic plastic fracture mechanics
$ESE(T)$	= eccentrically-loaded single edge crack tension specimen
$FCGR$	= fatigue crack growth analysis software

---

<sup>1</sup> University of Maryland Undergraduate, USRP Intern, Structural Engineering Division, Materials and Processes Branch, Lyndon B. Johnson Space Center

<sup>2</sup> Mechanical Engineer, JSC Structural Engineering Division, Materials and Processes Branch, 2101 NASA Parkway, Houston, TX 77058 / Mailcode ES4.

<sup>3</sup> Mechanical Engineer, JSC Structural Engineering Division, Materials and Processes Branch, 2101 NASA Parkway, Houston, TX 77058 / Mailcode ES4.

## I. Introduction

The electron beam free form fabrication (EBF3) additive manufacturing technology is a layer additive process where metal is placed in only areas of interest. As such the EBF3 process has several advantages over conventional manufacturing and machining techniques. The deposition technique of the EBF3 process reduces the need for raw materials, eliminates the need for cutting fluids, and substantially minimizes post fabrication waste. The technological capabilities of the EBF3 process make it desirable for space-based applications particularly on long duration missions beyond low Earth orbit. Additionally, the EBF3 process could provide feasibility of reconstructing spare parts on demand whereby resupply from earth is difficult<sup>1</sup>. This resolves the dilemma of transporting limited gear on long duration space missions due to mass and volume constraints during launch.

In order to demonstrate the structural capabilities of the EBF3 built hardware, part geometries were manufactured, machined into coupons and tested for strength, fatigue and fracture toughness. The EBF3 materials tested were from commonly used aerospace alloys. 2219 aluminum was chosen due to its high fusion weldability and prevalent use on the International Space Station. 316 stainless steel was chosen for its high tensile strength and fracture toughness. The electron beam free form fabricated parts were evaluated based on anisotropic properties and the results were compared to minimum design values. Fracture toughness, fatigue crack growth, and tensile tests were conducted to assess the mechanical properties of the EBF3 manufactured part geometries. Metallography was further conducted to examine the effects of the layer additive welding process on material micro-structure as well as its strength and toughness properties.

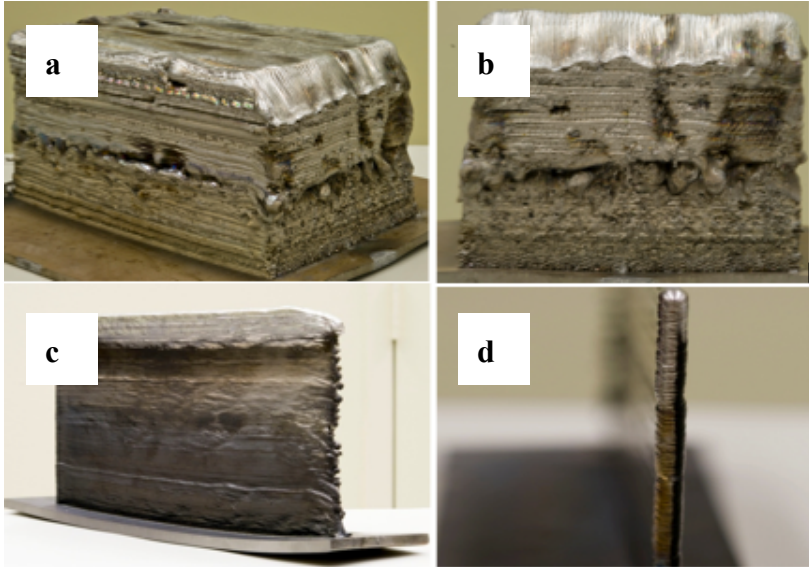


**Figure 1 EBF3 samples built at NASA Langley Research Center.** a) 10''x5''x5'' 2219 Al block b) 2219 Al multiple EBF3 bead passes – longitudinal view c) EBF3 316 stainless steel 9.8''x0.2''x4.8'' d) 316 single EBF3 bead pass – longitudinal view

## II. Nondestructive Evaluation

Prior to utilizing costly screening techniques, EBF3 part geometries were visually inspected and evaluated based on finish quality, weld appearance, and layer height accuracy. Visual inspection results from the 2219 aluminum block and 316 stainless steel thin wall in the as deposited condition revealed numerous surface anomalies and voids (Figure 1a and Figure 2). Upon visually inspecting the EBF3 aluminum and stainless steel parts, tensile and fatigue crack growth testing specimens were machined at different orientations. A series of radiography tests were then employed on 55 tensile coupons and 18 fatigue crack growth specimens to examine the material quality. The radiography results of the EBF3 stainless steel specimens sectioned perpendicular and parallel to the direction of deposition revealed no cracks, voids, porosity, or lack of fusion lines. Figure 4 demonstrates a decently welded electron beam free form fabricated 316 stainless steel tensile specimen that was sectioned parallel to the direction of metal deposition.

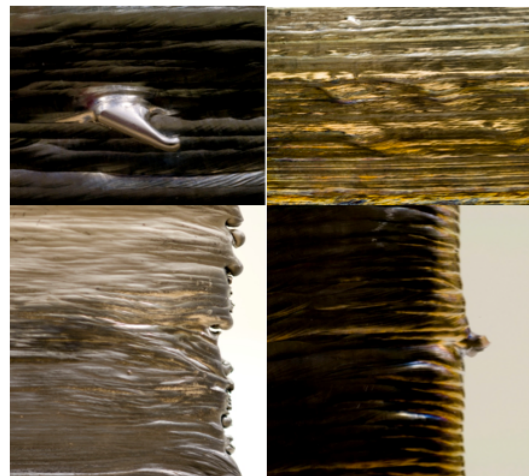


**Figure 2 EBF3 316 stainless steel surface anomalies**

Radiography results of 2219 aluminum specimens sectioned perpendicular to the direction of deposition demonstrated several discontinuities. The deposition parameters of the electron beam and the ability of aluminum to shrink by 12.5% upon solidification<sup>2</sup> were considered possible contributors to such defects. The radiography results of a few 2219 aluminum samples revealed several white spots that noted the presence of denser material than aluminum (Figure 4). An energy dispersive spectroscopy analysis on a few EBF3 2219 aluminum specimens, indicated high concentrations of copper parts disintegrated from the 2219 aluminum alloy which were delineated as white spots under the radiograph. This is expected in alloys with more than 5.5% copper and can also be seen in fusion welds.

In order to conduct a complete nondestructive screening of fatigue crack growth specimens and detect further flaws, other nondestructive techniques were employed. The use of radiography alone was insufficient since flaw orientations parallel to the direction of the x-ray beam or located at different angles were difficult to be detected. Supplementary screening techniques such as eddy current and ultrasound were therefore integrated to accurately detect subsurface cracks and flaws at different angles. The significance of conducting further non-destructive evaluation on fatigue crack growth specimens was to understand crack growth behavior in an event of crack deflection from the notch and be able to measure true crack growth length.

A piezo-electric crystal probe capable of transmitting high frequency waves was used to detect flaws through ultrasound inspection. The technique was capable of detecting additional flaws that were previously unnoticed in the radiography images. Eddy current inspection method was also employed to detect smaller subsurface cracks in the vicinity of the EDM notch. For this inspection method, a probe with an alternating current in a coil was used to generate a magnetic field and produce an eddy current when exposed to the surface of the metallic specimens. In the presence of the magnetic field, the existing specimen voids behaved as insulators and disrupted the magnetic field across the metal. As a result of this field discontinuity, voids were detected by a rapid pulse signal generated on an output screen. Overall, multiple inspection methods increased the probability of detecting critical flaws and allowed for a proper screening of EBF3 specimens.

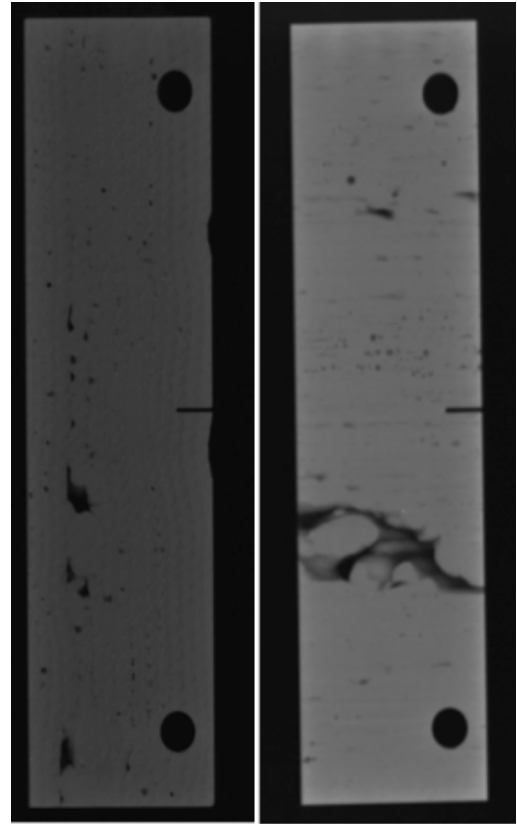


**Figure 3 Radiographs of ESE(T) EBF3 2219 aluminum fatigue crack growth specimen.** *Left – T-S orientation contained many voids, Right T-L orientation displayed lack of fusion lines*

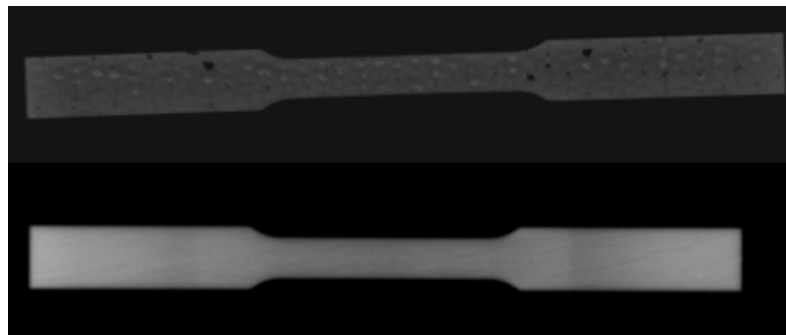


**Figure 4 EBF3 tension specimens.** *Top – 2219 aluminum with voids delineates disintegrated copper parts as white spots. Bottom – No discontinuities were observed in the 316 stainless steel specimen*

### III. Mechanical and Materials Testing

A series of mechanical and metallurgical tests were conducted to evaluate the capabilities and micro structural properties of the EBF3 material. Ten specimens were machined from the 316 stainless steel wall (5 L and 5 S) and 45 tensile coupons were machined from the 2219 aluminum block (10 L, 12 L-T, 5 S, 12 diagonal). Additionally, 18 fatigue crack growth specimen were machined and tested from the 2219 EBF3 block (8 L-T, 7 T-L, 3 T-S). The anisotropic tensile properties of the EBF3 2219 aluminum and 316 stainless steel specimens were evaluated. The metallography results and tensile properties were then compared to conventionally manufactured material. The mechanical tests conducted were integral to the Materials Verification and Validation process in demonstrating an EBF3 part for spaceflight.

#### A. Tensile Testing for Strength

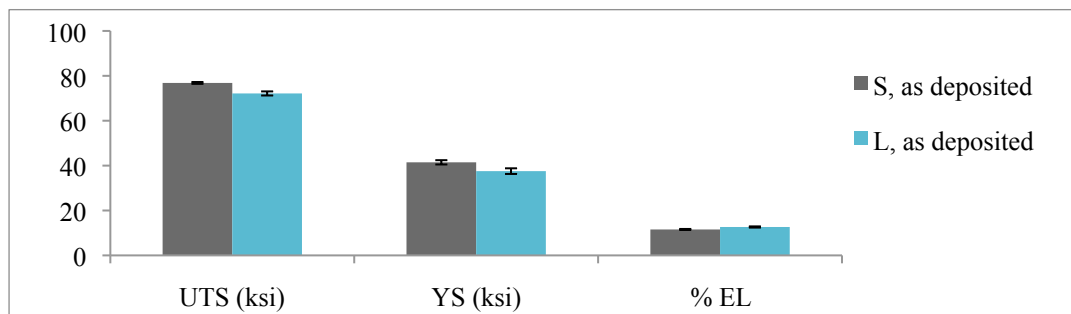
Numerous tension tests were conducted to observe the strength and effects of uniaxial loading on the electron beam fabricated 2219 aluminum and 316 stainless steel specimens. ASTM E8-E standard for tension testing was used to set up the tests and configure the EBF3 specimens. The ARAMIS® camera system was used to digitally detect changes in specimen displacement and measure localized deformation in the specimen gage area. 2219 aluminum flat dog-bone tensile specimens of 0.25” thickness were machined at different orientations from the EBF3 aluminum block. Stainless steel specimens of 0.097” thickness and 4” length were machined at different orientations from the EBF3 stainless steel thin wall. All tensile specimens were pulled to failure and data from the nominal loads versus percent strain were recorded.

##### 1. Specimen Configuration

To minimize the effects of residual stresses during testing, 400 grit sandpaper was used to remove the recast layer formed from melted and vaporized metal during electric discharge machining. The surface of the specimen gage area was sprayed with acrylic resin based black and white sprays to create a stochastic pattern. This allowed the ARAMIS cameras to assign coordinates to the pixilated facets and record localized deformation in the gage area. The specimens were installed in a load frame and the ARAMIS cameras were calibrated.

##### 2. Results

Based on the ASTM Specification E8-09, Standard Test Methods for Tension Testing of Metallic Materials<sup>3</sup>, fractured tensile samples near the grip and neck are omitted. Ultimate tensile strength, yield strength and ductility results were obtained from 2219 EBF3 aluminum and 316 stainless steel samples (Figure 5). The anisotropic properties of the 316 stainless steel specimens in the as fabricated condition were evaluated. Specimens were pulled across the EBF3 layers (S) and along the direction of deposition (L). The results in the short-transverse direction ( $\sigma_{\text{mean}} = 76.8$  ksi,  $n = 5$ ) demonstrated a 6.5% increase in tensile strength compared to specimens pulled in the longitudinal direction ( $\sigma_{\text{mean}} = 72.1$  ksi,  $n = 4$ ). The results also indicate no significant differences in ductility values (Table 1). Error bars in the longitudinal direction for tensile strength yield strength, and ductility were 0.91ksi, 1.26ksi, and 0.26 respectively. The error bars in the short-transverse direction were 0.42ksi, 0.95ksi, and 0.23.

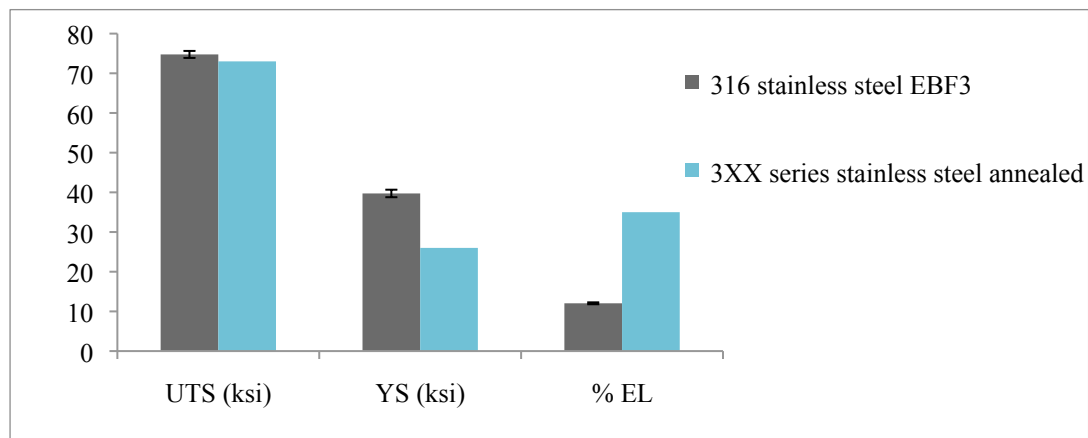


**Figure 5 EBF3 316 stainless steel anisotropic properties** *Short-transverse: across the layers. Longitudinal: along the direction of deposition*

**Table 1 EBF3 316 stainless steel anisotropic tensile data**

	L	S
Ultimate (ksi)	72.1	76.83
0.2% Yield (ksi)	37.5	41.4
% Elongation	12.6	11.5

Upon evaluating the anisotropic properties of the 316 stainless steel specimens in the as deposited condition, the mean tensile properties were obtained and compared to the properties of 300 series stainless steel in the annealed condition (Figure 6). The results demonstrated a marginal 2.3% increase in EBF3 tensile strength, and a 52.7% increase in yield properties ( $\sigma_{\text{yield}} = 39.7$  ksi,  $n = 9$ ) compared to the annealed condition ( $\sigma_{\text{yield}} = 26$  ksi). However, the 316 stainless steel specimens in the as fabricated condition demonstrated a 60% significant decrease in ductility. The differences between the two orientations reveal mildy anisotropic properties. The error bars for ultimate tensile strength yield strength, and ductility were 0.88ksi, 0.95ksi, and 0.24 respectively.

**Figure 6 EBF3 316 stainless steel tensile data and minimum design properties****Table 2 Comparison of EBF3 and conventionally manufactured stainless steel data**

	EBF3 316 stainless steel	Stainless steel annealed
Ultimate (ksi)	74.7	73
0.2% Yield (ksi)	39.7	26
% Elongation	12	30

Microstructural analysis of 316 stainless steel specimens in the as deposited condition indicated similarities to stainless steel microstructure in the annealed condition. Numerous metallographic images of 316 stainless steel specimens in the as deposited condition (Figure 8) displayed an array of hexagonal structures that was similar to stainless steel microstructure in the annealed condition (Figure 7). One noticeable difference between the two conditions was that stainless steel in the annealed condition had finer grain size compared to the as deposited condition. It was thought that the electron beam's low deposition rate during fabrication had contributed to this difference in grain size. Although, the two conditions displayed significant differences in grain size, the microstructures were very similar. These microstructural similarities have contributed to similar tensile properties between the EBF3 and the annealed conditions (Table 2). Further metallography analysis of 316 stainless steel specimens indicated that the layer additive deposition process did not disintegrate any metallic elements from the alloy.



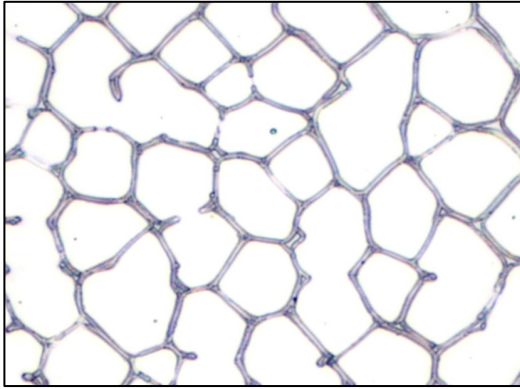


**Figure 8 EBF3 316 stainless steel microstructure (20x).** Etched with oxalic acid

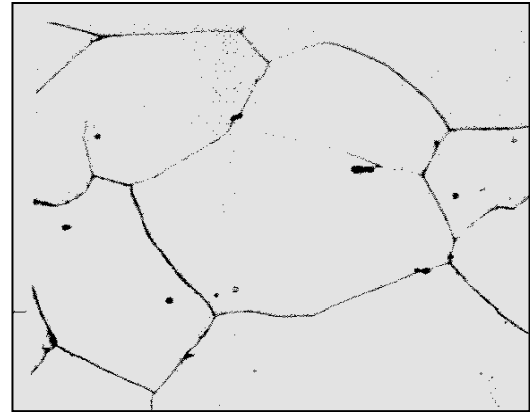


**Figure 7 Annealed 316 stainless steel (500x).<sup>4</sup>**

After obtaining tensile results from the EBF3 316 stainless steel specimens, the tensile and microstructural properties of 2219 aluminum parts were evaluated. Visual inspection results of the 2219 aluminum tensile specimens revealed shear fracture and brittle surfaces, which was expected from 0.25" thick aluminum material. An ANOVA analysis of variance revealed significant differences between the 2219 aluminum anisotropic tensile properties in the as fabricated condition. Specimens pulled parallel to the direction of deposition (L) had significantly higher tensile strengths than specimens pulled perpendicular to the multiple bead passes (L-T), layers (S), and at 45° angles (Diag.). This was expected since tensile strengths are typically higher in the longitudinal direction than the long transverse directions. The tensile specimens machined perpendicular to the EBF3 layers ( $\sigma_{\text{mean}} = 21.8$ , ksi,  $n = 5$ ) had significantly lower tensile properties than longitudinal ( $\sigma_{\text{mean}} = 37.78$ , ksi,  $n = 10$ ), long –transverse ( $\sigma_{\text{mean}} = 27.34$ , ksi,  $n = 12$ ) and diagonal ( $\sigma_{\text{mean}} = 28.63$ , ksi,  $n = 12$ ) orientations at a level of significance  $p = 1.2E-07$ .

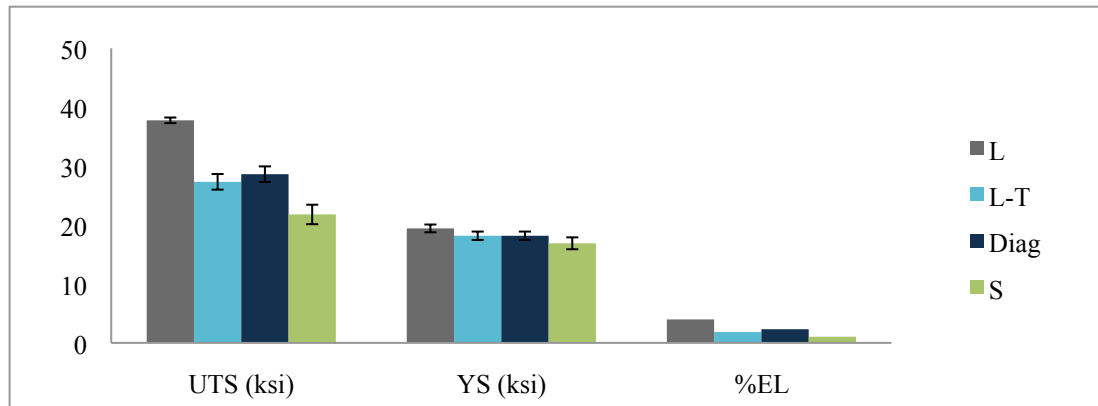


**Figure 9 Anisotropic tensile properties for 2219 aluminum**

**Table 3 Anisotropic tensile data for as deposited 2219 aluminum**

	L	L-T	Diagonal	S
Ultimate (ksi)	37.78	27.34	28.63	21.80
0.2% Yield (ksi)	19.43	18.18	18.18	16.90
% Elongation	3.98	1.84	2.32	1.04

The inconsistent tensile strength values were due to differences in microstructural properties at those orientations. The EBF3 layer-additive deposition process had re-heated previously deposited 2219 aluminum material. This event had affected the grain size at subsequent layers and influenced the EBF3 2219 anisotropic

tensile properties. The microstructure results indicated that the grain size discrepancy had also affected the aluminum ductility at different orientations. The ductility values from specimens tested along the direction of deposition (L) and across the EBF3 layers (S) differed by a factor of 4 (Table 3). Further results indicate no significant differences in the yield properties of EBF3 2219 aluminum tested in different orientations.

The mean tensile properties of the EBF3 2219 aluminum were then compared to conventionally welded and un-welded 2219 aluminum in the T87 condition. The results show that the 2219 aluminum in the as deposited condition had comparable ductility values to conventionally welded aluminum in the T87 condition (Table 4). The 2219 aluminum tensile and yield strength values in the as deposited condition had decreased by 27.5% and 41% respectively. The EBF3 tensile data also displayed a significant decrease in tensile properties when compared to minimum design values of 2219 aluminum in the T87 condition. The ultimate tensile strength, yield strength and ductility values had decreased by 52.8%, 64.6%, and 75% respectively. The EBF3 2219 aluminum error bars for the tensile strength, yield strength, and ductility were 1.06 ksi, 0.40 ksi, and 0.33 respectively. The tensile data for EBF3 2219 is significantly different since the material is in the as deposited, F-temper condition .

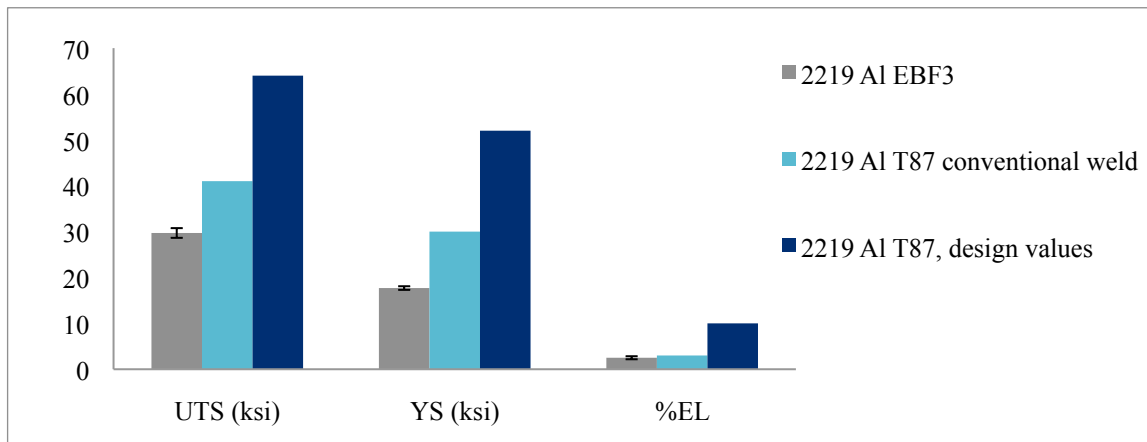


**Figure 10 Comparison of 2219 aluminum tensile properties in the as deposited and heat-treated conditions**

**Table 4 Tensile properties of 2219 aluminum in the as deposited and heat treated conditions**

	2219 as deposited, F temper	2219 T87, as welded	2219 T87, minimum design values
Ultimate (ksi)	29.70	41	63
0.2% Yield (ksi)	17.7	30	50
% Elongation	2.51	3	10

To further analyze the numerical tensile comparisons, a series of metallography tests were then employed to examine the microstructure properties of the 2219 aluminum in the as deposited condition as well as the properties of conventionally welded aluminum. The microstructure images from 2219 aluminum in the as deposited condition revealed discrepancies in grain size, partly caused by a thermal gradient as subsequent EBF3 layers were deposited (Figure 12). The non-uniform grain-size had contributed to low tensile strength and a 75% decrease in ductility compared to minimum design values. Welding had induced residual stresses but the decrease in 2219 aluminum tensile properties in the as fabricated condition were due to the materials non-uniform microstructure.



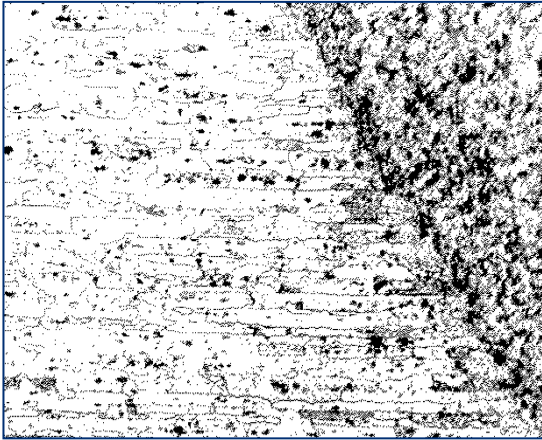


**Figure 11** Edge of fusion zone of a 2219 aluminum electron beam conventional weld.

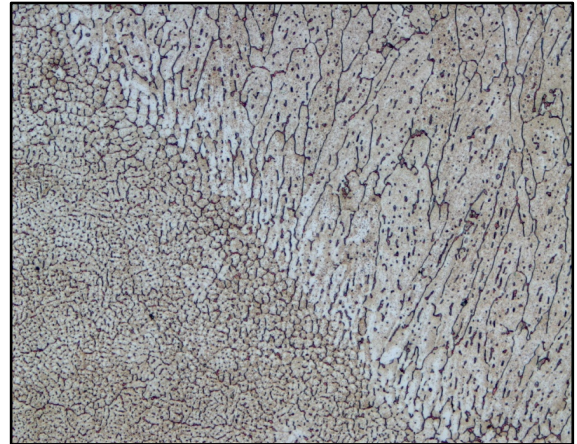


**Figure 12** EBF3 2219 aluminum weld. (Keller's reagent) *The different grain size is caused by the solidification rate*

Metallography images of 2219 aluminum in the as deposited condition had indicated comparable grain size and microstructure to conventionally welded 2219 aluminum (Figure 11). These similarities between microstructures have also contributed to similarities in material ductility (Table 4). Conversely, the EBF3 tensile properties were significantly lower than conventionally welded 2219 aluminum due to the EBF3 layer additive welding process that had reheated material and altered its grain size. A parameter that affected the microstructure of deposited material was the deposition rate of the electron beam gun. The low deposition rates had changed material solidification rates across the layers of the 2219 aluminum block. This occurrence had influenced the overall grain structure and decreased the tensile properties of the 2219 aluminum specimens in the as deposited condition.

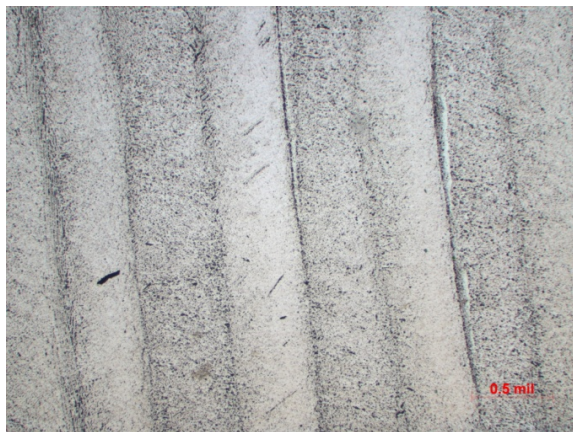


**Figure 13** EBF3 2219 aluminum 2219, as polished. *The metallograph displays bands of disintegrated copper between the bead passes*

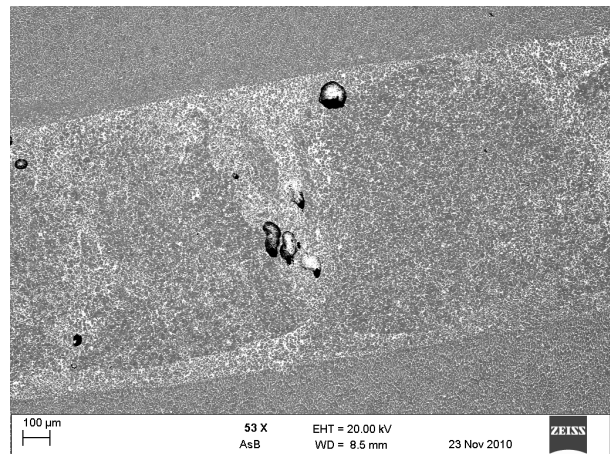


**Figure 14** SEM backscatter image of a magnified portion of a bead pass.

The low deposition rates in addition contributed to the excessive diffusion of copper between the weld beads of the 2219 aluminum block (Figure 13). An Energy Dispersive Spectroscopy analysis further demonstrated high concentrations of disintegrated copper parts that were delineated as white spots in the SEM image (Figure 14). Ductility values were also influenced by the disintegration of copper parts from the 2219 aluminum alloy specimens. The tensile data and metallography results of the 2219 aluminum and 316 stainless steel parts indicate that future process parameters need to be adjusted to achieve high quality EBF3 parts for space flight.

## B. Fatigue Crack-Growth Testing

Increased amplitude vibrations in materials induce cracks, cause fatigue and lead to fracture. Therefore, an understanding of the stress field concentration caused by an initiated flaw, and the crack propagation behavior is essential in determining the fatigue life of an EBF3 material. The FTA fatigue crack growth software uses equation (1) to sinusoidally vary the stress of the material with an amplitude  $\sigma_a$  of

$$\sigma_a = \frac{\Delta\sigma}{2} = \frac{\sigma_{\max} - \sigma_{\min}}{2} \quad (1)$$

and a mean stress  $\sigma_m$  of

$$\sigma_m = \frac{\sigma_{\max} + \sigma_{\min}}{2} \quad (2)$$

where  $\Delta\sigma$  is the peak-to-peak range over which the stress varies<sup>5</sup>. The upper and lower stress limits are defined by an R ratio, which includes the maximum and minimum applied stresses:

$$R = \frac{\sigma_{\min}}{\sigma_{\max}} \quad (3)$$

Fatigue crack growth is studied by cyclically loading a specimen containing a crack of length,  $a$ . The cyclic stress intensity range is defined as:

$$\Delta K = \frac{K_{\min}}{K_{\max}} = \Delta\sigma\sqrt{\pi a} \quad (4)$$

Below a certain cyclic stress intensity range, the crack growth rate approaches zero and the crack stops propagating. Above the threshold stress intensity value  $K_{th}$ , the fatigue crack growth rate  $da/dN$  increases linearly as the range  $\Delta K$  increases with time under constant cyclic stress. The Paris Law describes this steady state regime as:

$$\frac{da}{dN} = A\Delta K^m \quad (5)$$

where  $K$  and  $m$  are constants. At a  $\Delta K$  above the linear region, the crack growth rate accelerates until it approaches a critical stress intensity factor  $K_c$  that causes the material to fracture.

### 1. Specimen Configuration

Fatigue crack growth specimens were machined to eccentrically-loaded single edge crack tension specimen ESE(T), and chamfered to distribute nominal loads, and prevent bending and cracking at the specimen pin holes. The fatigue specimens were configured to ASTM E647-08 standard test method for measurement of fatigue crack growth rate<sup>6</sup>. Thin metal foil gages of 15mm in length were used as transducers to measure potential drop across the specimens and record crack length data. The fatigue crack growth specimens were configured for testing in the following process:

- The specimen gage area was polished with 400 grit sand paper
- Specimens were then cleaned with isopropyl alcohol to remove the recast layer debris
- 15mm KRAK-GAGE®s were aligned with the specimen notch using a microscope
- Heat-activated epoxy was applied and the gage backing was removed to affix the specimens
- Specimens were then covered with Teflon sheet and placed in pressure jigs
- The jigs were positioned in an oven to cure the epoxy at 85°F for 90 minutes
- Wires were then soldered on the gage to obtain data acquisition values (Figure 16)

- A multimeter was used to measure the resistance across the gages and to check for short circuits
- The reverse surface of the specimens was polished with 9 micron diamond paste to obtain a mirror finish surface and visually record crack extension lengths during testing

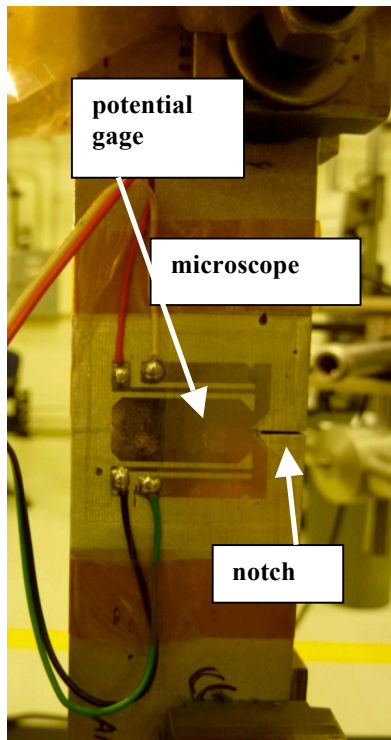


**Figure 15** A gaged ESE(T) 2219 EBF3 aluminum specimen. The specimens were loaded in tension-tension



**Figure 16** Fatigue crack growth test set-up. Specimens were loaded in servo-hydraulic loading frame of 5.5 kip capacity.

## 2. Test Conditions

Fatigue crack growth specimens were installed in a computer controlled servo-hydraulic loading frame of 5.5 kip capacity (Figure 15). The specimens were subject to a stress ratio of  $R=0.1$  with a maximum cyclic load of 425 lbs at a maximum cyclic rate of 90Hz. All specimens were subject to constant amplitude cyclic loading and constant stress ranges. Specimens were initially pre-cracked at an approximate cyclic stress intensity factor of  $\Delta K=3.81 \text{ ksi}\sqrt{\text{in}}$ . Once the pre-crack length was obtained the crack was propagated at an increasing crack growth rate to obtain data in the linear crack propagation region. Upon reaching the maximum desired crack length, the crack extension was artificially stopped and the specimens were statically loaded to failure. The average temperature and percent humidity during testing was 75 °F and 50% respectively. The specimens were sealed in plastic bags with dry air to minimize the effects of humidity on crack growth behavior and data acquisition readings. Visual measurements were taken upon pre-crack cycling and during crack propagation to measure and compare crack lengths with data acquisition values.



### 3. Data Analysis

Visual measurements were used to post-process data acquisition values and generate a set of adjusted crack length values using a modified secant (MS) combo from the FCGR Analysis software (Figure 17). The crack growth rate analysis was performed with a 7 point-MS combo method that used a 7-point incremental polynomial technique, with a modified secant method to generate additional data that would result in a smoother crack growth curve.

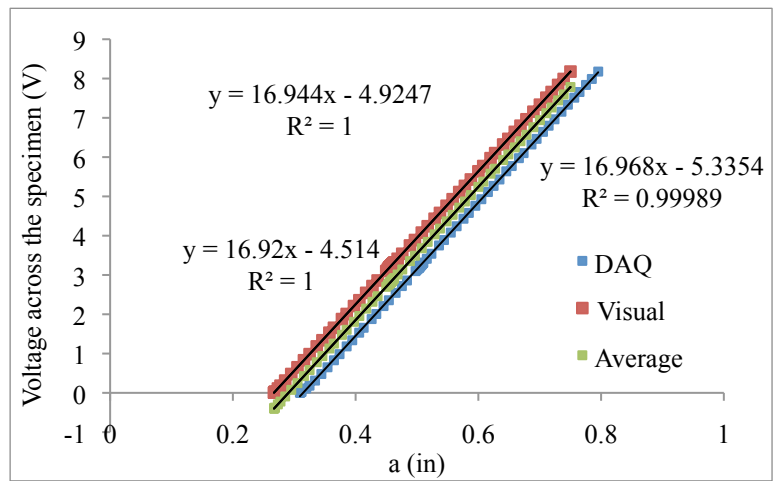


**Figure 17 Example of post processing DAQ and visual crack length values.** The crack length data were valid since there was a < 2% shift in the adjusted values

### 4. Results

Upon post processing the fatigue crack growth data, adjusted crack length values and corresponding load cycles were generated from the cyclic testing. In an EBF3 specimen with an initial flaw subject to a specific load, it was important to determine the total number of cycles the material endured prior to unstable crack growth. Anisotropic fatigue life curves from the EBF3 2219 aluminum material were generated (Figure 19) and the corresponding fracture surfaces were examined and compared to the numerical analysis (Figure 18). The results showed different fatigue life behavior for each orientation. A specimen in the T-L orientation revealed that a crack propagating parallel to the direction of metal deposition required a cycle count of approximately 800,000 cycles to induce unstable crack growth. Specimens in the L-T and T-S orientations where crack propagated across the bead passes and perpendicular to the EBF3 layers showed faster crack growth. The average cycle counts required to generate unstable crack growth in the L-T and T-S orientations were 100,000 and 300,000 cycles respectively. An analysis on both sides of the fractured specimen for the different orientations revealed that cyclic crack growth behavior was also influenced by the microstructure of the 2219 EBF3 material. Non-uniform grain structure and the presence of anomalies and voids have possibly contributed to decreased fatigue life specifically in the T-S and L-T orientations (Figures 18b, 18c respectively). Conversely, the fracture surface for the specimen in the T-L orientation revealed smooth crack propagation along the direction of deposition (Figure 18a) that resulted in slower crack growth and an increase in fatigue life.

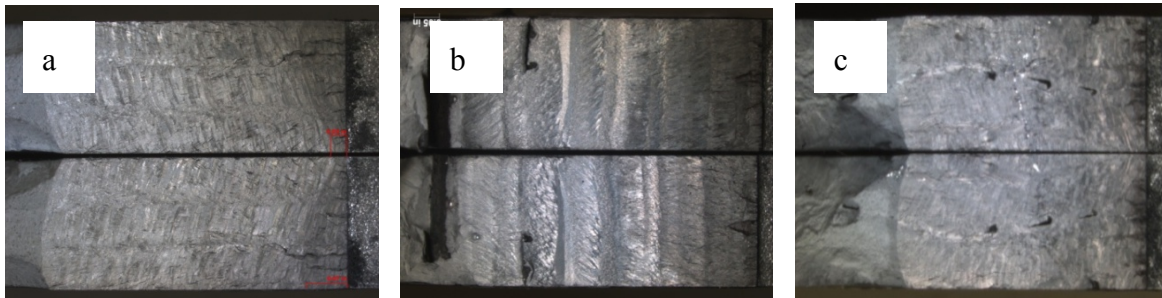


**Figure 18** The above images display both sides of fractured EBF3 2219 Al specimens and the direction of crack growth from the right (notch) side of the specimen to the left. a) T-L orientation displays smooth crack propagation along the direction of deposition. b) T-S orientation displays crack propagation behavior across the EBF3 layers. c) L-T orientation shows crack propagation across the bead passes

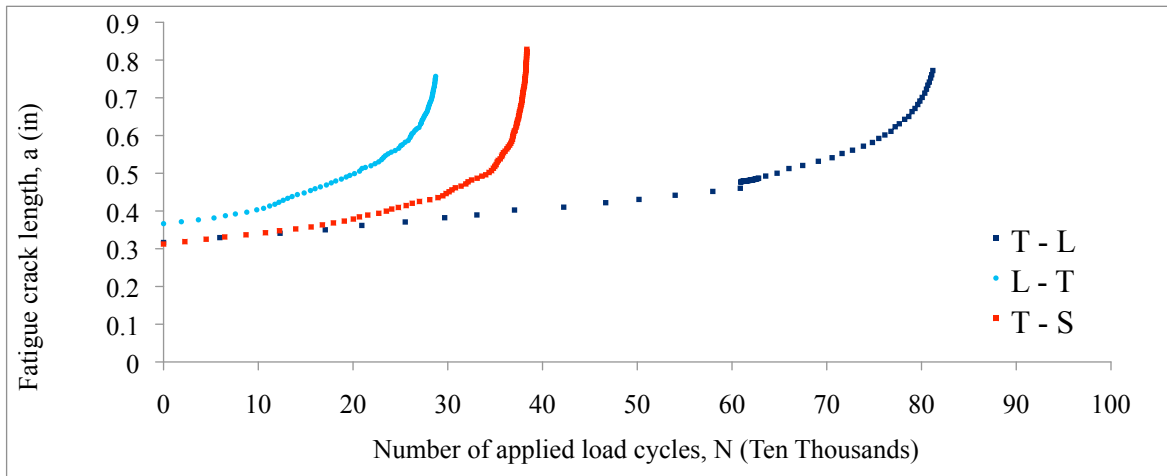


**Figure 19 Anisotropic fatigue life curves of 2219 EBF3 aluminum specimens under constant amplitude loading.**

Fatigue crack growth data was further obtained to analyze the behavior of the specimens under cyclic loading once a flaw was initiated. The log of crack growth rate per cycle,  $\log(da/dN)$  was plotted over the log of the cyclic stress intensity factor range,  $\log(\Delta K)$ . Anisotropic fatigue crack growth data for different specimens were obtained and their crack growth data were analyzed over  $\Delta K$  (Figure 20). The fatigue crack growth data showed similar crack growth behavior for orientations T-L and L-T in the steady state regime. The specimens in the T-S orientation demonstrated faster crack growth in the linear region due to the non-uniform microstructure across the EBF3 layers. The 2219 EBF3 aluminum was compared to conventionally welded aluminum in the T87 condition and heat-treated aluminum in the T62 condition. The steady state and unstable fatigue crack growth results of EBF3 2219 aluminum were comparable to properties of welded 2219 aluminum in the T87 condition. Failure for material in the as deposited condition occurred at a low cyclic stress intensity factor of  $\Delta K=22\text{ksi}\sqrt{\text{in}}$ ; whereas the heat-treated 2219 aluminum failed at a higher stress intensity range of  $\Delta K=50\text{ksi}\sqrt{\text{in}}$ . The data also indicated that a crack in an EBF3 sample propagated at a faster rate and failed at a lower cyclic stress intensity range than heat-treated aluminum.

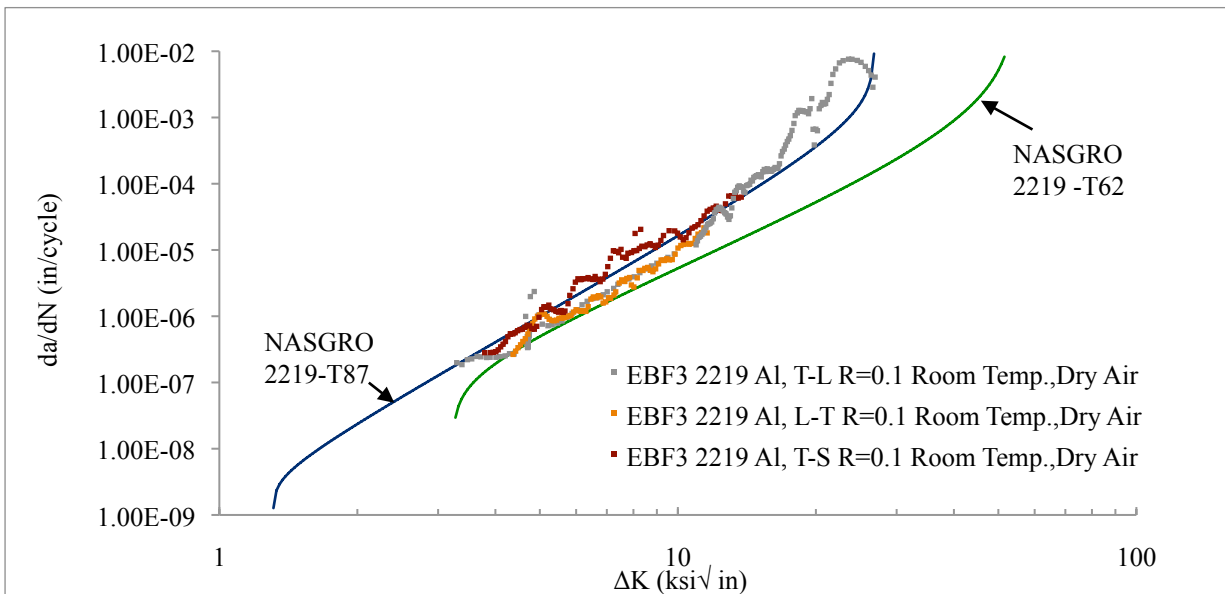


**Figure 20 Anisotropic fatigue crack growth data for EBF3 2219 aluminum in dry air  $R=0.1$ . The EBF3 material fails at a lower cyclic stress intensity factor than heat-treated aluminum;  $R=0.1$  Lab Air**

Based on the Metallic Materials Properties Development and Standardization handbook, in order to achieve the most complete derivation of fatigue-crack- propagation data,  $\Delta K$  values should be obtained from the threshold, steady state, and fast fracture regions. The MMPDS states data should include crack-growth rates as low as  $10^{-8}$  inches/cycle to clearly define the threshold range. Ideally, to properly document the effects of stress ratio, fatigue crack growth data should also be generated over a range of R ratios (i.e 0.1, 0.4, and 0.7). If possible, multiple heats of material should also be included<sup>7</sup>.

### C. Fracture Toughness Testing

Toughness is the resistance of a material to the propagation of a crack and is also a material dependent property. When a material cracks, it changes the uniform distribution of the nominal stress and creates localized stresses. The local stress ahead of a crack is defined as  $\sigma\sqrt{\pi a}$ , which is a measure of the intensity of the local stress. The quantity is also called mode 1 or tensile stress intensity factor  $K_I$ , which is a function of loading, crack size, and structural geometry. In a single edge notch  $K_I$  is defined as

$$K_I = 1.1\sigma\sqrt{\pi a} \quad ; (a \ll w) \quad (6)$$

where  $w$  is the width of the specimen and  $a$  is the flaw size. Unstable crack growth occurs when the stress intensity factor at a crack tip exceeds a critical value  $K_c$

$$K_I = K_c \quad (7)$$

and fracture occurs.

#### 1. Test Conditions

ESE(T) specimens from the 2219 aluminum material in the as deposited condition were placed in a computer based servo-hydraulic load frame of 10kip capacity. The samples were subject to constant amplitude cyclic loading and pre-cracked at a cyclic stress intensity factor of  $\Delta K=3.81$  ksi $\sqrt{\text{in}}$ . The cracks were propagated to a length of 0.8 inches and the cyclic loading was stopped to statically load the specimens to failure. Data from the final crack size  $a$ , peak failure load  $P$ , nominal stress  $\sigma$ , and specimen thickness  $t$ , were recorded and used to extract plane-stress fracture toughness values from the NASGRO material data processing software.

#### 2. Results

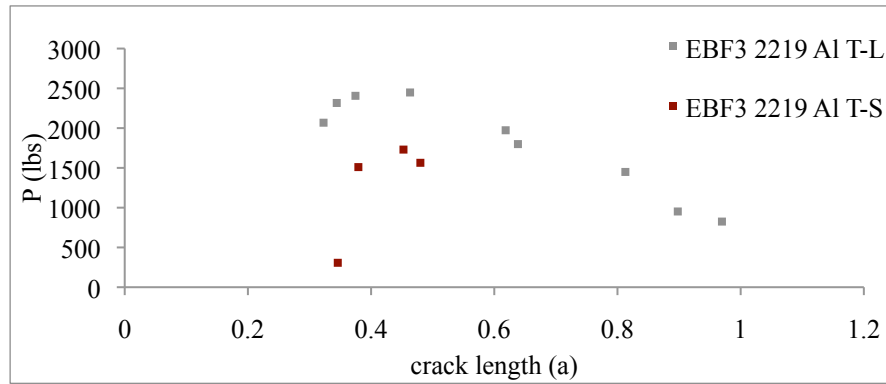
The results showed that the EBF3 2219 aluminum fracture toughness values slightly varied with grain direction (Table 5). Cracks had also been propagated to different lengths prior to fracture and revealed no significant differences in toughness values. Specimens in the T-L orientation endured a maximum load of 2448 lbs. prior to failure (Figure 22) but had marginally lower toughness values than the T-S orientation. The anisotropic results of the EBF2 2219 aluminum showed no significant difference in fracture toughness values obtained from different orientations. The properties of conventionally welded aluminum revealed that the fracture toughness of EBF3 2219 aluminum had decreased by 30% and was 3 times less than heat-treated 2219 aluminum in the T62 condition. Earlier tensile data revealed that low ductility in EBF3 2219 aluminum had contributed to low toughness values.



**Figure 21 Fracture surfaces of EBF3 2219 aluminum specimens demonstrated shear fracture upon failure**

**Table 5 Plane-stress fracture toughness values of EBF3 and heat-treated 2219 aluminum**

Material	Orientation	K <sub>c</sub> (ksi)
2219 EBF3	L-T	22.9
2219 EBF3	T-L	20.3
2219 EBF3	T-S	21.05
2219-T87 weld	L-T	29.8
2219-T62 heat treat	L-T	60.98

**Figure 22 R-curve for 2219 aluminum in the as deposited condition.**

The toughness data revealed that the EBF3 2219 material fractured above yield strength and abided by the linear elastic fracture mechanics criteria. All fractured fatigue crack growth specimens demonstrated ductile fracture along 45° planes through the specimen thickness. The fractured surfaces displayed single shear mode fracture due to an increase in plastic zone near the specimen crack tip as the crack propagated and developed plane stress<sup>8</sup>. This was expected since the crack tip deformation in thin specimens, occupy a large percentage of the specimen thickness, and the stresses were likely to behave in plane-stress rather than plane-strain.

#### IV. Summary

The microstructure of 316 stainless steel specimens in the as deposited condition resembled that of 300 series stainless steel in the annealed condition. The tensile results demonstrated a 52.7% increase in yield strength and a 60% decrease in ductility. The anisotropic results for the 316 stainless steel specimens revealed no significant tensile differences in the longitudinal and short-transverse orientations. The 2219 aluminum block in the as fabricated condition had similar microstructure and fatigue crack growth properties to that of conventionally welded aluminum in the T-87 condition. The metallography results of the 2219 EBF3 specimens had revealed some disintegrated copper elements from the aluminum alloy. As a result, this had contributed to a 75% decrease in ductility and a significant decrease in fracture toughness when compared to minimum design values. The tensile strength and ductility values of the 2219 specimens in the longitudinal direction were significantly higher than the tensile properties in the long-transverse, short-transverse, and diagonal orientations.

#### V. Conclusion

Deposition parameters such as electron beam power and travel speed need further adjusted to obtain optimum multiple pass part geometries. Upon the fabrication of an EBF3 part, a series of inspection methods need to be employed to properly obtain an overall nondestructive screening. Also, materials such as Inconel and 514-Aluminum will be utilized, built to different geometries, and tested to determine further capabilities of the EBF3 process and finalize an EBF3 part for spaceflight. Alloys with heat-treating components that take advantage of thermal cycling will be integrated to increase material strength. Alternative thermo-mechanical post processing techniques such as induction heat-treating will further be examined as a potential localized heat-treating technique in space.



## Appendix

Table 6 Example of EBF3 2219 aluminum fatigue crack growth data

Specimen: 2219ESE-TS-1-CG		Frequency = 90 Hz	R= 0.1		
Initial notch length (a) = 0.2661 in		W = 1.360 in	B = 0.250		
Total Cycles, N	K max	Crack length, a (in)	da/dN (in/cycle)	$\Delta K$ (ksi $\sqrt{\text{in}}$ )	
64,538	4.34	0.331	2.82E-07	3.90	
87,028	4.40	0.337	2.85E-07	3.96	
107,564	4.45	0.342	2.91E-07	4.01	
122,425	4.51	0.348	3.11E-07	4.06	
139,478	4.56	0.353	3.45E-07	4.11	
155,749	4.62	0.358	3.78E-07	4.16	
167,637	4.67	0.363	4.15E-07	4.21	
179,279	4.73	0.368	4.90E-07	4.26	
190,795	4.79	0.373	5.45E-07	4.31	
200,308	4.85	0.379	5.40E-07	4.37	
206,717	4.91	0.384	5.63E-07	4.42	
215,530	4.97	0.389	6.04E-07	4.47	
227,146	5.03	0.394	6.28E-07	4.53	
235,156	5.09	0.400	6.36E-07	4.58	
240,844	5.15	0.405	6.79E-07	4.63	
247,830	5.21	0.409	7.31E-07	4.69	
256,098	5.28	0.414	7.13E-07	4.75	
262,507	5.34	0.420	6.53E-07	4.80	
270,133	5.40	0.425	6.37E-07	4.86	
280,964	5.47	0.430	7.04E-07	4.92	
289,617	5.53	0.435	9.64E-07	4.98	
294,744	5.60	0.440	1.26E-06	5.04	
298,204	5.67	0.446	1.39E-06	5.10	
301,381	5.74	0.451	1.36E-06	5.17	
304,329	5.81	0.456	1.47E-06	5.23	
308,000	5.88	0.462	1.29E-06	5.29	
313,963	5.95	0.466	1.25E-06	5.36	
318,999	6.03	0.472	1.19E-06	5.42	
321,414	6.10	0.477	1.15E-06	5.49	
325,152	6.18	0.482	1.22E-06	5.56	
331,018	6.25	0.487	1.14E-06	5.63	
335,972	6.30	0.492	1.20E-06	5.67	
340,007	6.40	0.496	1.54E-06	5.76	
343,544	6.46	0.502	2.06E-06	5.81	
346,174	6.56	0.507	2.60E-06	5.91	
348,111	6.64	0.513	3.27E-06	5.98	
349,577	6.73	0.518	3.68E-06	6.05	
351,063	6.82	0.523	3.56E-06	6.14	
352,081	6.90	0.529	3.69E-06	6.21	
353,296	6.99	0.534	3.69E-06	6.29	
355,327	7.08	0.538	3.83E-06	6.37	
356,846	7.15	0.545	3.65E-06	6.44	
357,613	7.26	0.549	3.58E-06	6.53	
358,741	7.33	0.554	3.98E-06	6.60	
360,496	7.44	0.559	3.62E-06	6.69	
362,313	7.52	0.565	3.33E-06	6.77	
363,880	7.62	0.570	3.64E-06	6.86	

# NASA USRP – Internship Final Report

365,259	7.72	0.575	4.29E-06	6.95
366,449	7.81	0.580	5.60E-06	7.03
367,415	7.92	0.585	7.49E-06	7.13
368,257	8.04	0.590	9.75E-06	7.23
368,779	8.14	0.597	9.53E-06	7.32
369,051	8.25	0.601	9.08E-06	7.43
369,499	8.35	0.606	1.02E-05	7.52
370,190	8.42	0.611	7.77E-06	7.58
371,170	8.57	0.613	7.48E-06	7.71
371,997	8.65	0.622	8.94E-06	7.78
372,534	8.80	0.627	9.16E-06	7.92
372,970	8.91	0.632	9.75E-06	8.02
373,449	9.04	0.637	9.80E-06	8.13
374,091	9.16	0.642	1.05E-05	8.24
374,687	9.28	0.648	1.14E-05	8.35
375,071	9.42	0.653	1.12E-05	8.47
375,360	9.53	0.659	1.19E-05	8.57
375,793	9.67	0.663	1.24E-05	8.70
376,347	9.80	0.668	1.17E-05	8.82
376,788	9.93	0.674	1.09E-05	8.93
377,173	10.06	0.679	1.18E-05	9.06
377,702	10.20	0.683	1.39E-05	9.18
378,127	10.34	0.689	1.65E-05	9.30
378,360	9.15	0.694	1.78E-05	8.07
378,605	10.64	0.699	1.95E-05	9.57
378,870	9.41	0.704	2.05E-05	8.30
379,111	10.94	0.709	1.94E-05	9.84
379,331	11.09	0.714	1.79E-05	9.98
379,702	11.25	0.720	1.57E-05	10.12
380,179	11.42	0.724	1.43E-05	10.27
380,558	11.58	0.730	1.53E-05	10.42
380,873	11.75	0.735	1.82E-05	10.57
381,186	11.93	0.740	2.13E-05	10.74
381,409	12.11	0.745	2.25E-05	10.90
381,597	12.30	0.751	2.41E-05	11.07
381,799	12.48	0.756	2.77E-05	11.23
382,026	12.68	0.761	3.26E-05	11.41
382,213	12.88	0.767	3.85E-05	11.59
382,303	13.07	0.772	4.10E-05	11.76
382,409	13.28	0.777	4.31E-05	11.95
382,526	13.47	0.782	4.58E-05	12.12
382,634	13.68	0.787	4.00E-05	12.31
382,774	13.88	0.792	3.94E-05	12.49
382,958	14.11	0.796	4.97E-05	12.70
383,088	14.35	0.802	6.52E-05	12.91
383,136	14.57	0.809	6.53E-05	13.11
383,188	14.83	0.813	6.95E-05	13.35
383,266	15.05	0.818	6.07E-05	13.54
383,345	15.29	0.823	6.27E-05	13.75

### Acknowledgments

Y. Ekrami thanks the National Aeronautics and Space Administration and USRP coordinator, Venronica Seyl for providing this wonderful undergraduate research opportunity at the Johnson Space Center. The author is thankful of Scott C. Forth, Michael C. Waid, Royce Forman, Joachim Beek, John Figert, Daniel B. Garcia, Daila Gonzalez, Branch Chief Brad Files, Lucie Johannes, Daniel Rybicki, Leslie Schaschl, Jay Bennett, David Shindo, as well as laboratory technicians in the Metallurgy, NDE, and Structures Test Lab: Larry Graham, Frank Somonski, Michael Kocurek, Don Wilbanks, Ovidio Oliveras, Norm Ruffino, David Stanley, James Martinez and Julieta Ventura for their immense support and assistance on this project. The author gratefully acknowledges input from Karen M. Taminger and Robert A. Hafley at NASA Langley Research Center.

### References

---

<sup>1</sup> Taminger, Karen M.B., Hafley, Robert A., and Dennis, Dicus D, “Solid Freeform Fabrication: An Enabling Technology for Future Space Missions,” *International Conference on Metal Powder Deposition for Rapid Manufacturing San Antonio, TX*, 2002

<sup>2</sup> Viswanathan, Srinath. Apelian, Diran, DasGupta, Rathindra, Jorstad, John L., *ASM Metals Handbook Volume 15: Casting* ASM International, 2008. Print

<sup>3</sup> “Standard Test Methods for Tension Testing of Metallic Materials.” Vol. E8-E, 09 ed. West Conshohocken, PA: American Society for Testing and Materials, 2009.

<sup>4</sup> Vandervoot, George F., *ASM Metals Handbook Volume 9: Metallography and Microstructures* ASM International, 2008. Print

<sup>5</sup> Ashby, Michael, Shercliff, Hugh, Cebon, David. *Materials: Engineering, Science, Processing, and Design* University of Cambridge, UK Elsevier Ltd., 2007. Print

<sup>6</sup> “Standard Test Method for Measurement of Fatigue Crack Growth Rates.” Vol E647, 08 ed. West Conshohocken, PA: American Society for Testing and Materials, 2008.

<sup>7</sup> “Metallic Materials Properties Development and Standardization.” 04 ed, pp 2138-2189. Columbus, OH: Federal Aviation Administration, 2008.

<sup>8</sup> Broek, David. *The Practical Use of Fracture Mechanics*. FractuREsearch Inc. Dordrecht: Kluwer Academic Publishers, 1989. Print